Exploring Solar Wind Origins and Connecting Plasma Flows from the Parker Solar Probe to 1 au: Nonspherical Source Surface and Alfvénic Fluctuations

Olga Panasenco, Marco Velli, Raffaella D'amicis, Chen Shi, Victor Réville, Stuart D. Bale, Samuel T. Badman, Justin Kasper, Kelly E Korreck, J.W. Bonnell, et al.

The Astrophysical Journal Supplement Series, 246:54 (15pp), 2020 February https://doi.org/10.3847/1538-4365/ab61f4

Exploring Solar Wind Origins and Connecting Plasma Flows from the *Parker Solar Probe* to 1 au: Nonspherical Source Surface and Alfvénic Fluctuations

Olga Panasenco[1], Marco Velli[2], Raffaella D'Amicis[3,4], Chen Shi[2], Victor Réville[2,5], Stuart D. Bale[6,7,8,9], Samuel T. Badman[6,7], Justin Kasper[10], Kelly Korreck[11], J. W. Bonnell[7], Thierry Dudok de Wit[12], Keith Goetz[13], Peter R. Harvey[7], Robert J. MacDowall[14], David M. Malaspina[15], Marc Pulupa[7], Anthony W. Case[11], Davin Larson[7], Roberto Livi[7], Michael Stevens[16], and Phyllis Whittlesey[7]

[1] Advanced Heliophysics, Pasadena, CA, USA; panasenco.olga@gmail.com
[2] UCLA Earth Planetary and Space Sciences Department, Los Angeles, CA, USA
[3] National Institute for Astrophysics (INAF), Institute for Space Astrophysics and Planetology (IAPS), Via del Fosso del Cavaliere 100, I-00133 Rome, Italy
[4] Serco S.p.A, Via Sciadonna 24, I-00044 Frascati, Italy
[5] IRAP, Université Toulouse III—Paul Sabatier, CNRS, CNES, Toulouse, France
[6] Physics Department, University of California, Berkeley, CA 94720-7300, USA
[7] Space Sciences Laboratory, University of California, Berkeley, CA 94720-7450, USA
[8] The Blackett Laboratory, Imperial College London, London, SW7 2AZ, UK
[9] School of Physics and Astronomy, Queen Mary University of London, London E1 4NS, UK
[10] University of Michigan, Ann Arbor, MI, USA
[11] Smithsonian Astrophysical Observatory, Cambridge, MA, USA
[12] LPC2E, CNRS and University of Orléans, Orléans, France
[13] School of Physics and Astronomy, University of Minnesota, Minneapolis, MN 55455, USA
[14] Solar System Exploration Division, NASA Goddard Space Flight Center, Greenbelt, MD 20771, USA
[15] Laboratory for Atmospheric and Space Physics, University of Colorado, Boulder, CO 80303, USA
[16] Smithsonian Astrophysical Observatory, Cambridge, MA 02138, USA
Received 2019 September 23; revised 2019 December 11; accepted 2019 December 11; published 2020 February 3

Abstract

The magnetic field measurements of the FIELDS instrument on the *Parker Solar Probe* (*PSP*) have shown intensities, throughout its first solar encounter, that require a very low source surface (SS) height ($R_{SS} \leqslant 1.8\ R_{\odot}$) to be reconciled with magnetic field measurements at the Sun via potential field extrapolation (PFSS). However, during *PSP*'s second encounter, the situation went back to a more classic SS height ($R_{SS} \leqslant 2.5\ R_{\odot}$). Here we use high-resolution observations of the photospheric magnetic field (*Solar Dynamics Observatory*/Helioseismic and Magnetic Imager) to calculate neutral lines and boundaries of the open field regions for SS heights from 1.2 to 2.5 $R_{\odot}$ using an evolving PFSS model and the measured solar wind speed to trace the source of the wind observed by *PSP* to the low corona and photosphere. We adjust R_{SS} to get the best match for the field polarity over the period 2018 October–November and 2019 March–April, finding that the best fit for the observed magnetic field polarity inversions requires a nonspherical SS. The geometry of the coronal hole boundaries for different R_{SS} is tested using the *PSP* perihelion passes, 3D PFSS models, and LASCO/C2 observations. We investigate the sources of stronger-than-average magnetic fields and times of Alfvénic fast and slow wind. Only some of the strongly Alfvénic slow wind streams seen by *PSP* survive and are observed at 1 au: the origins and peculiar topology of the background in which they propagate is discussed.

Unified Astronomy Thesaurus concepts: The Sun (1693); Slow solar wind (1873); Alfven waves (23); Space plasmas (1544); Solar activity (1475); Solar magnetic fields (1503); Solar corona (1483); Fast solar wind (1872); Solar coronal holes (1484); Solar coronal mass ejections (310); Solar coronal streamers (1486); Solar filaments (1495)

Supporting material: animation

1. Introduction

The *Parker Solar Probe* (*PSP*; Fox et al. 2016) completed its first perihelion pass on 2018 November 6, reaching a distance of 35.7 $R_{\odot}$ from the Sun, closer by almost a factor of 2 than previous man-made explorations. Observations of the magnetic field and velocity show that *PSP* crossed the heliospheric current sheet multiple times (see Figure 1) and that the speed of the wind was predominantly very slow. Remarkably, the wind displayed a strongly dominant outward propagating spectrum of Alfvénic fluctuations throughout the encounter, a feature that is rarely seen in very slow solar wind streams at Earth and beyond.

Here we use the simplest possible magnetic field extrapolation, namely Potential Field Source Surface (PFSS) model, to locate the solar footpoints of the solar wind seen by *PSP* throughout its first perihelion passage. We then explore possible connections with the solar wind seen at L1 and at Earth and discuss the different, evolved properties of the solar wind seen at much greater distances in conjunction with the source regions on the Sun. PFSS extrapolations provide a qualitatively correct model of the overall topology of the magnetic field at the source surface (SS), but may place the neutral line and pseudostreamers at slightly different latitudes with respect to what is seen in coronagraph data (see, e.g., Morgan & Habbal 2010; Morgan 2011). We therefore supplement the information provided by PFSS with coronagraph images and other plasma properties, such as the presence of Alfvén waves propagating away from the Sun and the corresponding magnetic

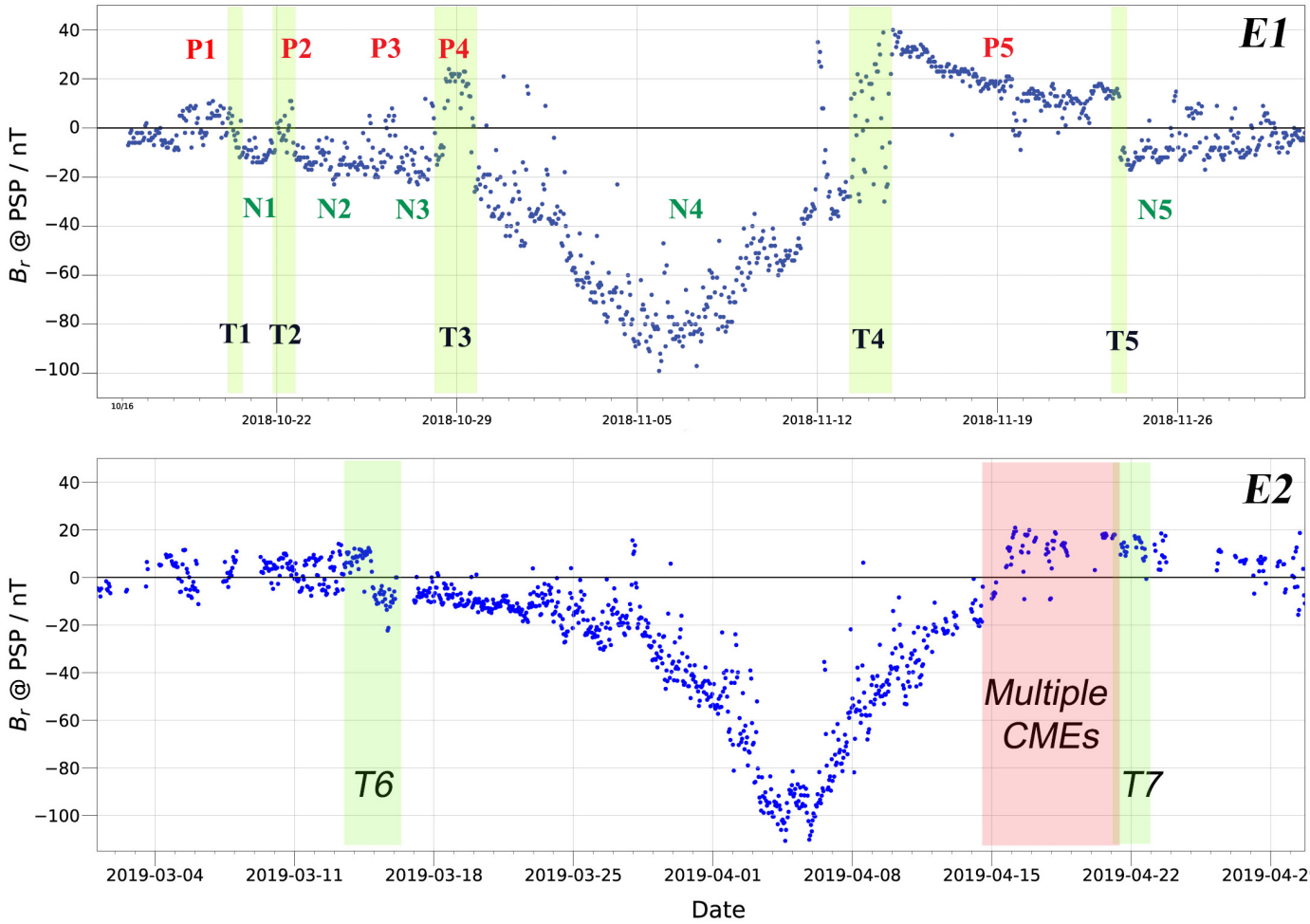

Figure 1. The B_r measurements for Encounters (1) and (2) (labeled *E1* and *E2*). Five positive (P1–P5) and five negative (N1–N5) periods were identified for *E1*, and one negative and two positive periods for *E2*. The transition periods of changing polarity are labeled T1–T7 and defined in Table 1. Multiple CMEs occurred during *E2*, the time period shaded in red.

field–velocity field correlation, to back up the correct determination of the neutral line crossings.

The first perihelion passages of *PSP* occurred during the minimum phase of the present solar cycle. During this phase, a spacecraft located in the ecliptic at 1 au would generally detect alternating streams of faster and slower wind. Beyond the speed differences, these two solar wind regimes show many other specific characteristics, from the large-scale structure (Schwenn 1990) to composition (Geiss et al. 1995), to the spectral properties of the embedded turbulent fluctuations (see reviews by Tu & Marsch 1995; Bruno & Carbone 2013) and last but not least, different origins on the Sun. In this regard, although it is well known that most of the fast solar wind streams originate from polar coronal holes, the origin(s) of the slow wind are still a mystery (e.g., Wang & Sheeley 1990; Antonucci et al. 2005; Abbo et al. 2016), and indeed, the classification of the solar wind outflow uniquely in terms of wind speed is probably too simplistic (e.g., von Steiger 2008; Zhao et al. 2009; Ko et al. 2018; D'Amicis et al. 2019; Stansby et al. 2019).

One important feature characterizing solar wind fluctuations, especially within the main portion of fast solar wind streams, is the presence of large-amplitude fluctuations showing an Alfvénic nature. The adjective Alfvénic refers to the presence in the wind of large-amplitude velocity and magnetic field fluctuations with the correlation between them corresponding to Alfvén waves propagating away from the Sun. In addition, relative density fluctuations are suppressed together with fluctuations in magnetic field magnitude, so that the magnetic field vector apex moves locally on the surface of a sphere (Matteini et al. 2015).

Based on this definition, fast wind is usually found to be more Alfvénic than slow wind (Belcher & Davis 1971; Belcher & Solodyna 1975). However, recent results (D'Amicis & Bruno 2015; D'Amicis et al. 2019) have shown that the slow solar wind can also sometimes show a high degree of Alfvénicity, with velocity and magnetic field fluctuations as large as those found in the fast wind. It is important to note that this kind of slow wind was studied using measurements at 1 au where one would expect a degradation of the Alfvénic correlation due to the solar wind expansion. In addition, the identification of this Alfvénic slow wind was found on a statistical basis over the maximum of solar cycle 23. D'Amicis et al. (2019) suggested the idea that a possible solar source for this Alfvénic slow solar wind would lie in low-latitude small coronal holes (in agreement with Wang 1994; Neugebauer et al. 1996; Wang & Ko 2019; Wang & Panasenco 2019) that were a ubiquitous feature of the solar surface during the maximum of solar cycle 23 (Platten et al. 2014).

An Alfvénic slow wind stream was observed in a portion of the wind preceding a fast stream during the perihelion passage

Table 1
Transition Periods for *E1* and *E2*, *PSP* B_r

Transition	Time Period (2018–2019)	Polarity
T1	Oct 20	P1/N1
T2	Oct 22	N1/P2/N2
T3	Oct 28–29	N3/P4/N4
T4	Nov 13–14	N4/P5
T5	Nov 23	P5/N5
T6	Mar 15	P/N
T7	Apr 22	N/P

of the *Helios* mission at solar activity minimum (Marsch et al. 1981). A detailed characterization of this kind of wind was developed recently by Stansby et al. (2020) and Perrone et al. (2020). In contrast to the findings of D'Amicis et al. (2019), the amplitude of the fluctuations was smaller in this case than that seen in typical fast wind but still larger than that of the typical slow wind. The solar wind seen by *PSP* over the first perihelion encounter appears to be an example of slow Alfvénic solar wind. In this case, the Alfvénic slow wind observed by *PSP* originated from a very rapidly expanding small equatorial coronal hole adjacent to a pseudostreamer configuration, i.e., a multipolar closed configuration opening into a unipolar field (Wang et al. 2007; Panasenco & Velli 2013; Panasenco et al. 2019). The corresponding solar wind at Earth showed this property only partially, providing evidence for the evolution and destruction of Alfvénicity in a slow solar wind stream as it traveled from the Sun to 1 au.

In the next section, the magnetic field measurements from the first *PSP* encounter and the connectivity from the solar coronal footpoints of *PSP* into the solar wind are discussed, and the SS height required to properly match the polarity transitions observed by the spacecraft and map them back to the Sun is determined. Although this height is lower than the "standard" accepted values, we show that it actually depends on the region above the Sun, along the lines of Levine et al. (1982). For clarity, we have labeled the polarities (P for positive, N for negative) and the transitions (T) we will discuss explicitly in Figure 1 (and further identified in Table 1). The choice of these transitions, seen in the figure as labeled green shadings over the 1 hr median field values plotted throughout the time intervals of the first (*E1*) and second (*E2*) encounters, was made to identify clear, reliable crossings of the heliospheric polarity inversion sheet, avoiding time-dependent disturbances such as blobs or coronal mass ejections (CMEs). For *E1*, we do not discuss the P3/N3 transition as there are multiple crossings within the 1 hr median time, and similarly for *E2* we limit the discussion to the two transitions T6 and T7. *E2* is discussed mainly to contrast the resulting SS height with the more surprising case of *E1*.

2. PFSS Reconstructions of the Solar Magnetic Field, Nonspherical Source Surface, and *PSP* Solar Wind Sources

In our study, we use the PFSS model developed by Schrijver & De Rosa (2003). As a lower boundary condition, this PFSS model incorporates magnetic field maps produced by an evolving surface-flux transport model based on magnetic fields observed by the Helioseismic and Magnetic Imager (HMI; e.g., Scherrer et al. 2012; Schou et al. 2012) on the *Solar Dynamics Observatory* (*SDO*). The model evolves these fields in accordance with empirical prescriptions for differential rotation, meridional flows, and convective dispersal processes. In addition to SS height, PFSS extrapolation depends crucially on the effective resolution of the fields on the solar disk and the treatment of the polar fields, which are difficult to observe and often not used directly by the PFSS extrapolation model itself (in the present case, the magnetogram assimilation window is limited to the area within $\pm 60^\circ$ of disk center, and polar fields are determined by the large-scale transport processes). The effective magnetogram resolution used for the extrapolations here is $8''$ ($\simeq$5800 km on the Sun, significantly less than a typical supergranule diameter). The PFSS model was updated in 2012 with polar flux transport modeling corrections to better fit the observed magnetic fields and neutral lines (Liu et al. 2012) of the next-to-last deep minimum. With a fixed resolution and the defined flux transport model, PFSS now depends only on the SS height. Again, the real coronal fields importantly involve dynamic layers, from the chromosphere through the transition region to the corona itself, where volume currents play a role and the PFSS model cannot be expected to reproduce the real solar coronal magnetic field precisely. It is for this reason that identifying the solar origin of solar wind parcels must rely on other factors as well, discussed further below.

Coronal heating and solar wind acceleration lead to the stretching and opening of magnetic field lines into the solar wind. The simplest models for the magnetic expansion consist of the PFSS model and its variants: a height is specified at which all magnetic field lines become open and radial—the SS height—typically located at a height $R_{SS} = 2.5\,R_\odot$ from the center of the Sun, and the field from the photosphere to the corona is reconstructed, on the basis of the radial field at the surface, as a potential field. The radius of the SS is a free parameter of the model. By construction, because the magnetic field in the shell between the photosphere and SS is potential, the magnetic field in that region falls as $1/R^3$ or faster, depending on the multipolar expansion, i.e., on the strength and distribution of magnetic polarities. On the other hand, beyond the SS, the field becomes radial and decays as $1/R^2$. As a consequence, adjusting the SS height changes both the total amount of open flux as well as the magnitude of the magnetic field at a given radius, and this can be done to fit the average values observed by different spacecraft. In addition, the location and shape of the heliospheric current sheet (HCS) will change. For example, Todd Hoeksema at Wilcox Solar Observatory has been producing HCS maps for two SSs: 2.5 and $3.25\,R_\odot$. Averaging over solar cycles, the best SS radius has been found to be at about $2.5\,R_\odot$, although $R_{SS} = 3.25\,R_\odot$ gave a slightly better result when comparing to the high-latitude *Ulysses* measurements during the 1994 polar pass in the middle of the declining phase. In this period, the Sun presents fewer sunspots but the global field may be stronger and more organized topologically. During the cycle 22 and 23 minimum periods, the SS radius values of $1.8\,R_\odot$ and $1.9\,R_\odot$ produced the best results (Lee et al. 2011). Badman et al. (2020) carries out an extensive investigation with PFSS reconstructions using different solar magnetic field sources (GONG, HMI). One of the main conclusions is that in order to accurately capture the relative magnitude of the radial magnetic field measured by *PSP*, and sufficiently open midlatitude and equatorial coronal holes, the SS must be placed at $R_{mSS} \leqslant 2.0\,R_\odot$. Levine et al. (1977), using data for the entire *Skylab* period in 1973, found that extrapolation of an average magnetic field strength in the equatorial plane at 1 au, which is near the observed

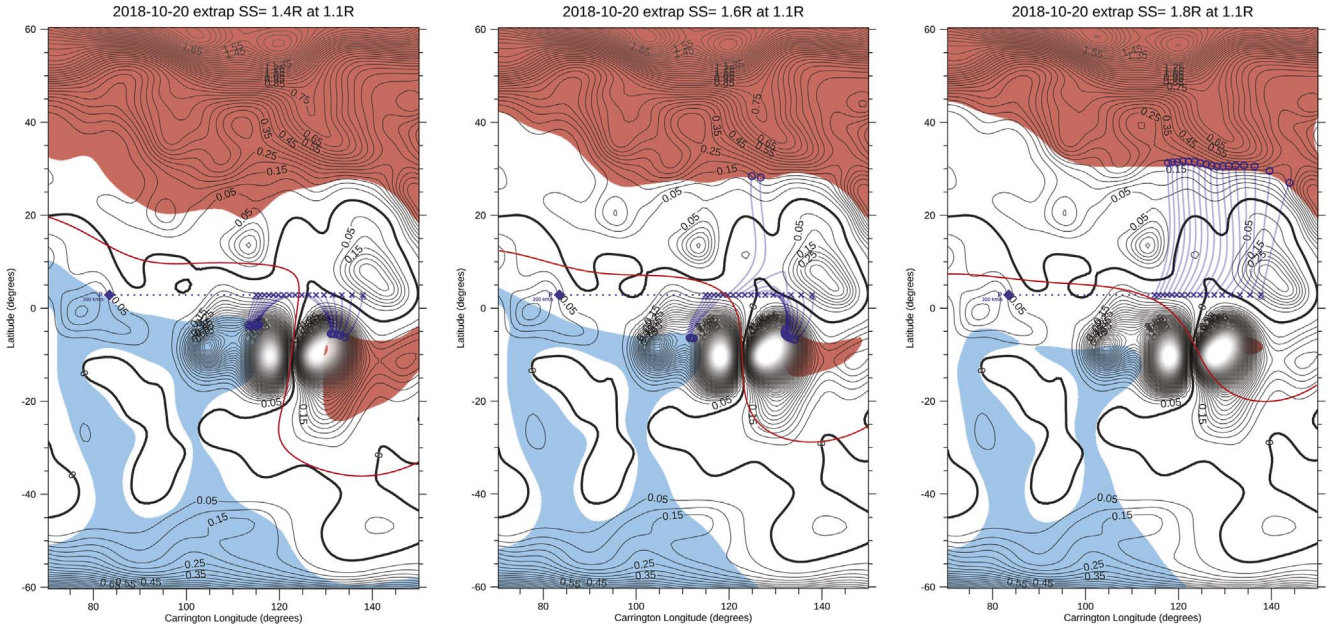

Figure 2. PFSS B^2 contour maps and magnetic field line footpoints for *PSP* for polarity transition period T1. The projection of the *PSP*'s location (blue diamond) is projected onto the source surface (blue crosses) and down to the solar wind source region (blue circles) calculated for the height $R = 1.1 R_\odot$ and solar wind speeds of 300 ± 80 km s^{-1} (in increasing/decreasing steps of 10 km s^{-1}). From left to right, $R_{SS} = 1.4, 1.6, 1.8\ R_\odot$. Open magnetic field regions are shown in blue (negative) and red (positive), the neutral line at $R = 1.1 R_\odot$ is in bold black, while the SS neutral line is shown by the thin red line.

average value, requires an SS near 1.5 $R_\odot$ during the cycle 20 minimum. The present cycle 24 solar minimum is also very weak, and indeed as we shall see, the optimal SS height will also be quite low.

The *PSP*/FIELDS (Bale et al. 2016, 2019) observations of the radial magnetic field are summarized in Figure 1, showing the intensity and sign of the field expressed in terms of the modal field value from bins comprising 1 hr of data (i.e., each data point is the modal value of $B_r \pm 30$ minutes), so that all the rapidly varying transient structures are removed. In the figures, the label N is used to identify periods of negative polarity, P for different periods of positive polarity, and T for the transition periods (not all, but those of interest, as specified in Table 1). One can see that from October 18 through November 26 the polarity of the field changed at least seven times, while throughout the whole of the perihelion pass, from October 30 through November 15, *PSP* found itself in a region of negative polarity.

In the overall weak field of the current solar minimum during the first encounter, we can identify two specific areas on the Sun with a magnetic field stronger than average: the new active regions NOAA AR 12724 and AR 12725 at Carrington longitude ~125°, and a decaying and heavily dispersed AR 12713 (first emerged five rotations earlier) at Carrington longitude ~320°.

In the following, the footpoints of the wind seen by *PSP* will be traced down to their source regions on the Sun and compared with the magnetic field polarity at a height of 1.1 $R_\odot$ as obtained by PFSS extrapolation with different SS heights. In order to trace *PSP* observations to the sources back at the Sun, a ballistic extrapolation using the wind speed measured at *PSP* down to the SS height is carried out, at which point individual PFSS field lines are traced down toward the Sun. To analyze the robustness of this prediction, corrections up to ± 80 km s^{-1}, in bins of 10 km s^{-1}, are added onto the measured solar wind velocity, and the ballistic tracing is repeated for all speeds. The result, for the transition period T1, is illustrated in Figure 2. The plots show magnetic pressure isocontours at 1.1 $R_\odot$, with

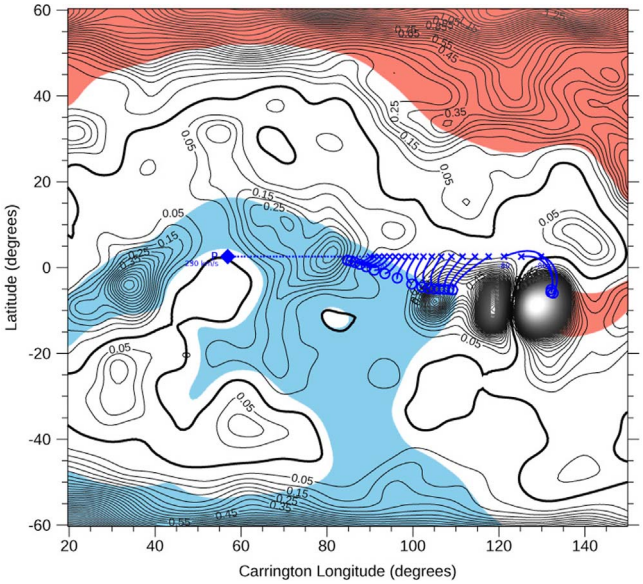

Figure 3. PFSS B^2 contour maps and solar wind footpoints along *PSP*'s trajectory for polarity transition period T2. The projection of *PSP*'s location (blue diamond) on the source surface (blue crosses) and down to the solar wind source region (blue circles) calculated for the height $R = 1.1 R_\odot$ and solar wind speed 230 ± 80 km s^{-1}. The projection calculated for the $R_{SS} = 1.6\ R_\odot$. Open magnetic field regions shown in blue (negative) and red (positive); the neutral line is in bold.

shaded color indicating coronal holes with the respective polarity (blue, negative and red, positive). Overplotted is the direct radial projection of *PSP*, as a blue diamond, while the the ballistic extrapolations down to the SS are shown by the blue crosses on the plot.The crosses are then traced down to 1.1 $R_\odot$ using the PFSS field lines, and the results are plotted as open circles. The first thing to note is how irregular the neutral line (in bold) is, with large latitudinal excursions, the height of the SS notwithstanding (for the three panels, from left to right,

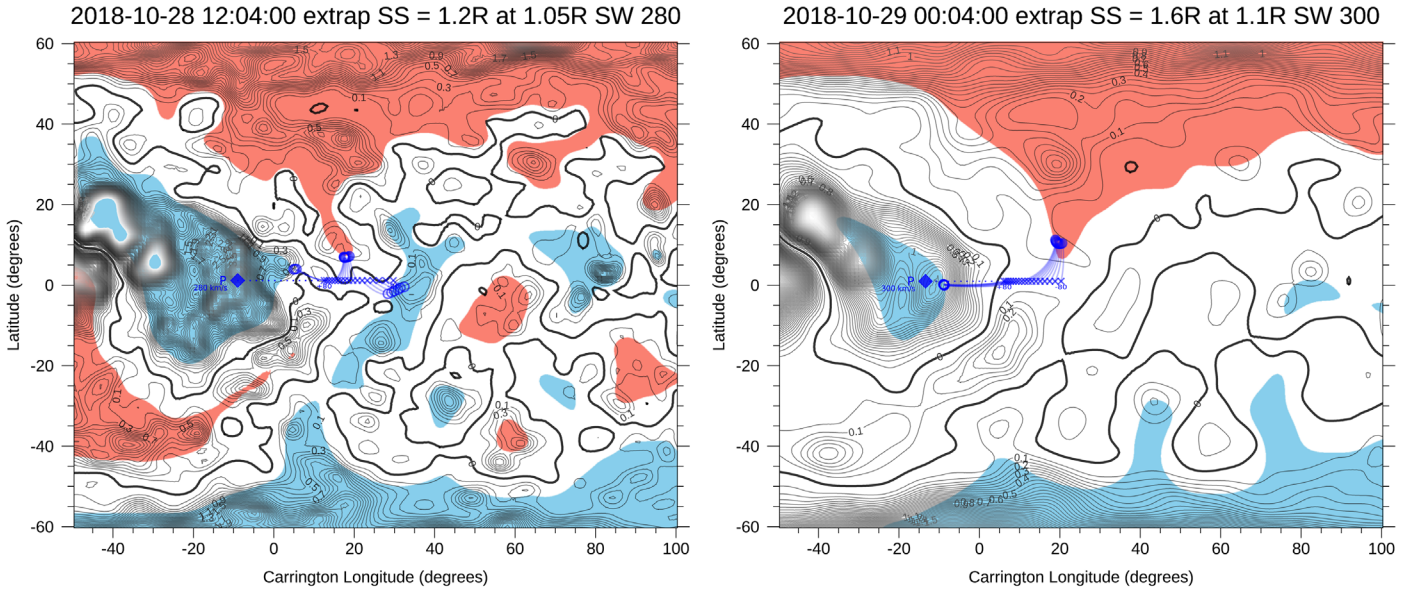

Figure 4. PFSS B^2 contour maps and solar wind footpoints along *PSP*'s trajectory for polarity transition period T3. The projection of *PSP*'s location (blue diamond) on the source surface (blue crosses) and down to the solar wind source region (blue circles) calculated for the height $R = 1.05.R_{\odot}$ and solar wind speed 280 (left) and 300 (right) $\pm$ 80 km s^{-1}. The maps and projections calculated for $R_{SS} = 1.2\ R_{\odot}$ (left, transition N3/P4) and $R_{SS} = 1.6\ R_{\odot}$ (right, transition P4/N4). Open magnetic field regions shown in blue (negative) and red (positive); the neutral line is in bold.

R_{SS} goes from 1.4 to 1.8 $R_{\odot}$). As the SS moves upward, coronal holes shrink in size, as seen from the decreasing areas shaded in blue and red moving from the left to the right panel. By inspecting the different panels, one can see that the SS height of 1.8 $R_{\odot}$ (right panel) cannot correctly identify the transition from one polarity to the other as seen in interval T1; rather, *PSP* then remains connected to the positive polarity of the low boundary of the polar coronal hole at higher latitudes. On the other hand, lower SS heights show that small changes in solar wind speed lead to a quick transition from one polarity to the other (left and center panels). The best fit for T1 is $R_{SS} = 1.6\ R_{\odot}$. Figures 3–7 provide analogous plots for the polarity transitions labeled T2–T7.

Figure 3 illustrates the T2 transition from negative to positive and back, N1/P2/N2. An R_{SS} height of 1.6 $R_{\odot}$ was used to reproduce the negative–positive–negative jump, as *PSP*'s trajectory moves leftwards on the plot. For the period T2, *PSP* magnetic footpoints were located mostly in the negative open field regions N1 and N2. To reproduce the observed short jump back to the positive polarity P2, the solar wind speed of 230 $\pm$ 80 km s^{-1} was used, reproducing the short-lived magnetic connection back to the positive polarity region, which is the observed P2 result. The positive region P2 is the same as P1 in Figure 2.

Figure 4 illustrates transition T3 (N3/P4/N4), when the *PSP* magnetic footpoints moved across very weak magnetic field regions with $B_r = 0.4$–1.3 G at 1.1 $R_{\odot}$, which is at least an order of magnitude smaller compared to the near-equatorial magnetic field observed during the solar maximum in cycle 24 in 2014 (Figure 5 in Janardhan et al. 2018). To reproduce the polarity transition observed by the *PSP*/FIELDS instrument, the R_{SS} height is reduced to 1.2 $R_{\odot}$. The left panel in Figure 4 illustrates the transition T3 (from negative to positive polarities): the *PSP* magnetic footpoints connected to the small equatorial coronal hole with negative polarity (blue shade) and to the open field area of the polar coronal extension of positive polarity (red shade). The right panel shows the transition P4/N4: the negative polarity region N4 is the western boundary of the big equatorial coronal hole above which *PSP* will spend the following two weeks: 2018 October 30–November 15. For the N3 negative polarity region, the SS was lowered to $R_{SS} = 1.2\ R_{\odot}$ and field lines projected from the SS down to $B_r = 1.05\ R_{\odot}$. The transition N3/P4 is especially sensitive to the SS height and easily disappears for higher R_{SS}. However, the transition P4/N4 is captured for R_{SS} up to 1.6 $R_{\odot}$. This conclusion is also supported by Badman et al. (2020).

Figure 5 illustrates the protracted transition period T4 (N4/P5), during which *PSP* leaves the corotation region above the negative open field area to which the spacecraft was connected for the two previous weeks. Figure 1 shows that the duration of the transition period T4 is 2 days and twice as long as all simple polarity transitions. To investigate the longer period transition, the *PSP* magnetic footpoint projections were modeled for two consecutive days 2018 November 14–15 and for three different R_{SS} heights of 1.6, 1.8, and 2.0 $R_{\odot}$. The goal was to find the R_{SS} height required to connect *PSP* to both polarities N4 and P5. The top-left panel in Figure 5 shows the moment when the *PSP* footpoints are located entirely in the negative area $R_{SS} = 1.6$, $R_{\odot}$: the beginning of the transition period T4. Twelve hours later (top-right panel), the transition is in progress and *PSP* connects to both polarities when including solar wind speed fluctuations up to $\pm$80 km s^{-1}. To establish the best fit and the maximum fit, the SS was brought farther all the way up to $R_{SS} = 2.0\ R_{\odot}$ (Figure 5, bottom-left panel) and found that the transition was lost. Therefore, the bottom-right panel in Figure 5 shows the modeling for $R_{SS} = 1.8\ R_{\odot}$ made for the next day, 2018 November 15, the maximum workable SS height for this region.

Figure 6 illustrates the transition T5 (P5/N5), which was fast (hr) and without polarity fluctuations. This can be explained by the fact that *PSP* was flying farther from the Sun, no longer in the quasi-corotation regime as it had been over T3 and T4, which are the beginning and end of the corotation. The simplicity of the transition period T5 allowed the straightforward modeling of the footpoint connection to opposite polarities of the relatively weak magnetic field area. The left

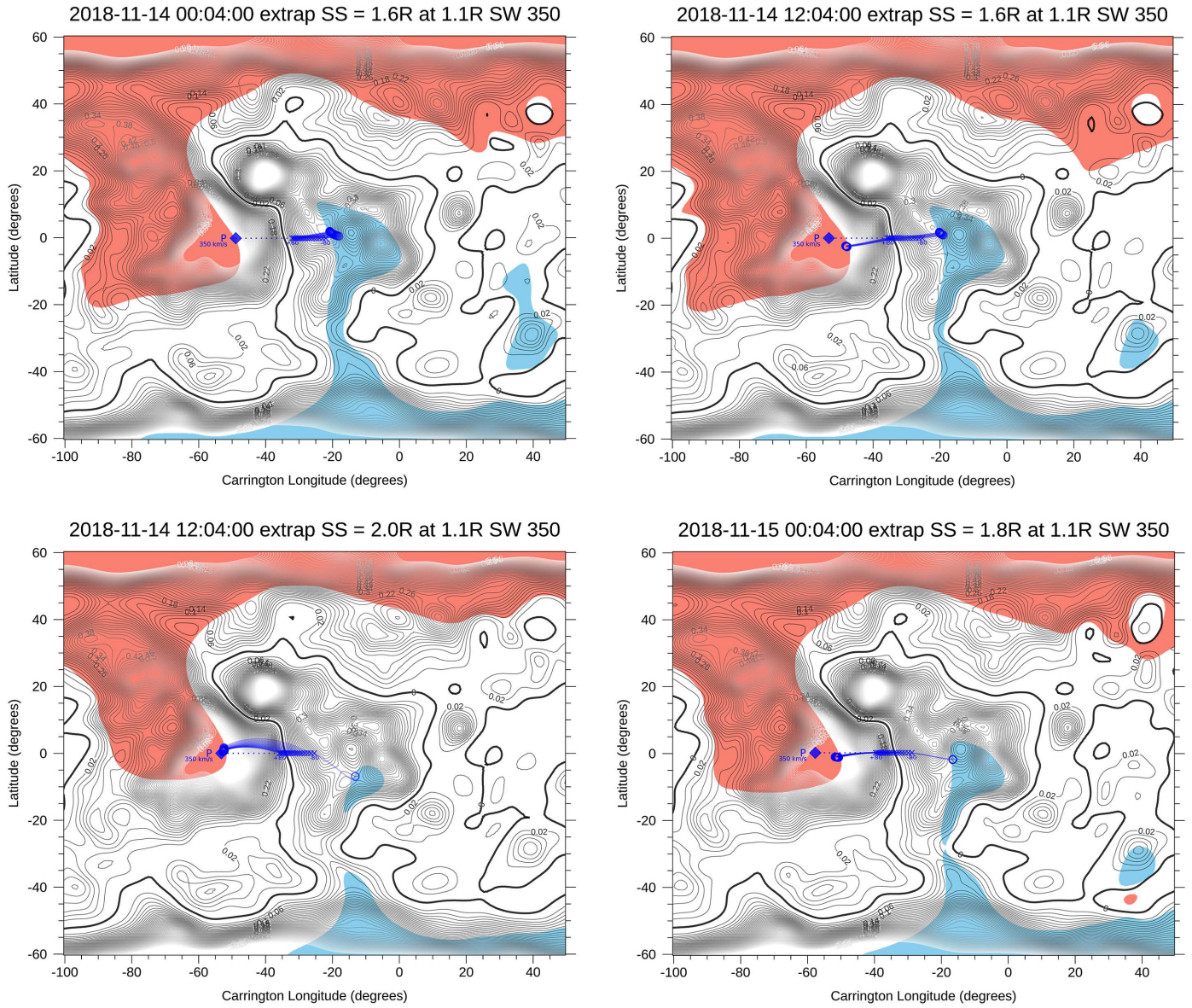

Figure 5. PFSS B^2 contour maps and solar wind footpoints along *PSP*'s trajectory for the polarity transition period T4. The projection of *PSP*'s location (blue diamond) on the source surface (blue crosses) and down to the solar wind source region (blue circles) calculated for the height $R = 1.1 R_\odot$ and solar wind speed 350 ± 80 km s^{-1}. The maps and projections calculated for three moments of time and three different R_{SS}. From left to right, top to bottom, $R_{SS} = 1.6$, 1.6, 2.0, and 1.8 $R_\odot$. Open magnetic field regions shown in blue (negative) and red (positive); the neutral line is in bold.

panel shows the optimal *PSP* connection with both polarities for $R_{SS} = 1.4\ R_\odot$; the right panel shows how this transition nearly disappeared when the SS height increased up to $R_{SS} = 1.6\ R_\odot$.

Figure 7 illustrates the transitions T6 and T7 during *E2*. Polarity transition T6 was also fast (hr) again because *PSP* was flying farther from the Sun and not in corotation. The left panel in Figure 7 shows the *PSP* connection with both positive and negative polarities calculated for $R_{SS} = 1.8\ R_\odot$. The right panel in Figure 7 shows the polarity transition T7 across the very strong active region NOAA AR 12738 on 2019 April 22. The SS height was found to be $R_{SS} = 2.5\ R_\odot$. This transition was preceded by multiple CMEs originating from the AR. These created a series of magnetic field inversions observed by *PSP* and indicated in Figure 1 (bottom panel). How CMEs influence *PSP* connections is discussed in the following Section 2.1.

Table 2 summarizes results for the best estimates of the solar SS height R_{SS} above the polarity transition regions along *PSP*'s trajectory during the first encounter. The best fit is defined as the height R_{SS} of the SS when the modeled magnetic polarity transition corresponds to that observed by *PSP* for the given T, even considering variations in the solar wind velocity. The upper limit value for R_{SS} is the height at which the calculated solar magnetic footpoints of *PSP* begin to deviate from the observed polarity values. $B_{1.1}$ in Table 2 is the photospheric magnetic field value B_r projected to 1.1 $R_\odot$ by PFSS modeling. $B_{1.1}$ is tabulated for the regions on the Sun where the corresponding polarity transitions (T1–T7) were taking place.

During the current minimum, the optimal R_{SS} for PFSS reconstruction is found to be smaller right above polarity inversion regions, corresponding to dips in the overall nonspherical SS shape. The concept of a nonspherical SS was introduced by Schulz et al. (1978) and developed further by Levine et al. (1982). Using our results for the best-fit R_{SS} above the polarity transition regions T1–T7, a nonspherical SS shape was constructed in correspondence with the *PSP* solar

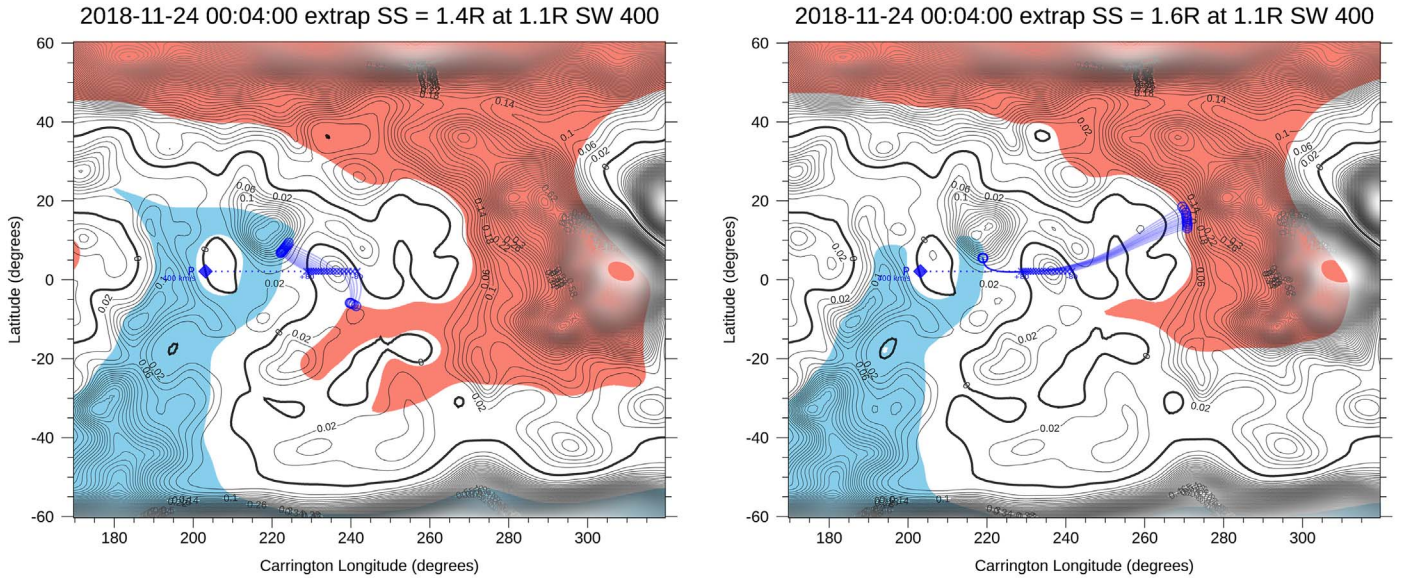

Figure 6. PFSS B^2 contour maps and solar wind footpoints along *PSP*'s trajectory for polarity transition period T5. The projection of *PSP*'s location (blue diamond) on the source surface (blue crosses) and down to the solar wind source region (blue circles) calculated for the height $R = 1.1\ R_\odot$ and solar wind speed 400 ± 80 km s^{-1}. The maps and projections calculated for the different R_{SS}. From left to right, $R_{SS} = 1.4$ and $1.6R_\odot$. Open magnetic field regions shown in blue (negative) and red (positive); the neutral line is in bold.

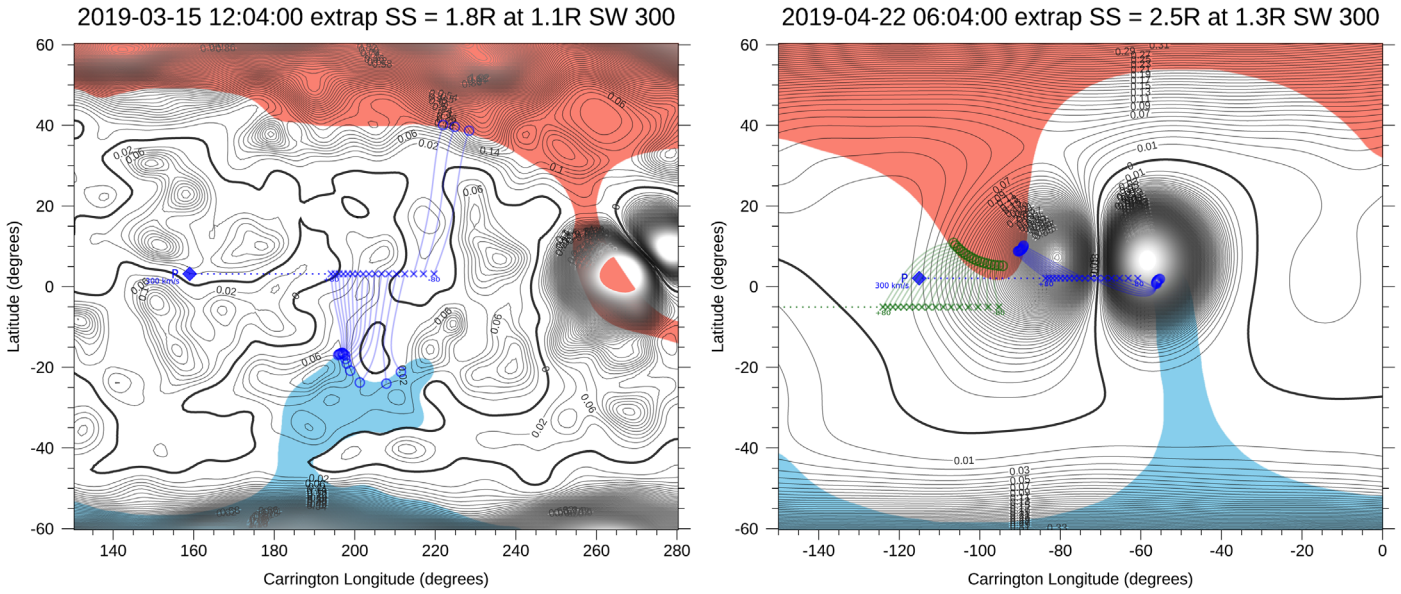

Figure 7. PFSS B^2 contour maps and solar wind footpoints along *PSP*'s trajectory for polarity transition periods T6 (left) and T7 (right). The projection of *PSP*'s location (blue diamond) on the source surface (blue crosses) and down to the solar wind source region (blue circles) calculated for the height $R = 1.1\ R_\odot$ and solar wind speed 300 ± 80 km s^{-1}. The maps and projections calculated for the different R_{SS}. From left to right, $R_{SS} = 1.8$, $2.5R_\odot$. Open magnetic field regions shown in blue (negative) and red (positive); the neutral line is in bold. Earth projections to SS and below shown in green color.

Table 2
Source Surface Height above T1–T7 (in $R_\odot$)

	T1	T2	T3.1	T3.2	T4	T5	T6	T7
R_{SS}	1.4	1.4	1.2	1.6	1.6	1.4	1.6	2.5
R^*_{mSS}	1.6	1.6	1.3	1.8	1.8	1.5	1.8	2.5
$B_{1.1}$, G	1.8–2.2	1.4–2	0.2–0.4	1.2–1.4	0.6–1.2	0.2–0.4	4.0	30 (sunspot)

Note. R_{SS}—best fit, R^*_{mSS}—max, $B_{1.1}$ is B_r at 1.1 $R_\odot$.

encounter. The result is show in Figure 8, where the local minima in R_{SS} above T1–T7 are connected with continuity to the higher SS positions elsewhere using quadratic and cubic Bézier curve interpolations. The striking difference in the resulting shapes can be attributed to the different magnetic field magnitudes at the photosphere. The SS, contracted and

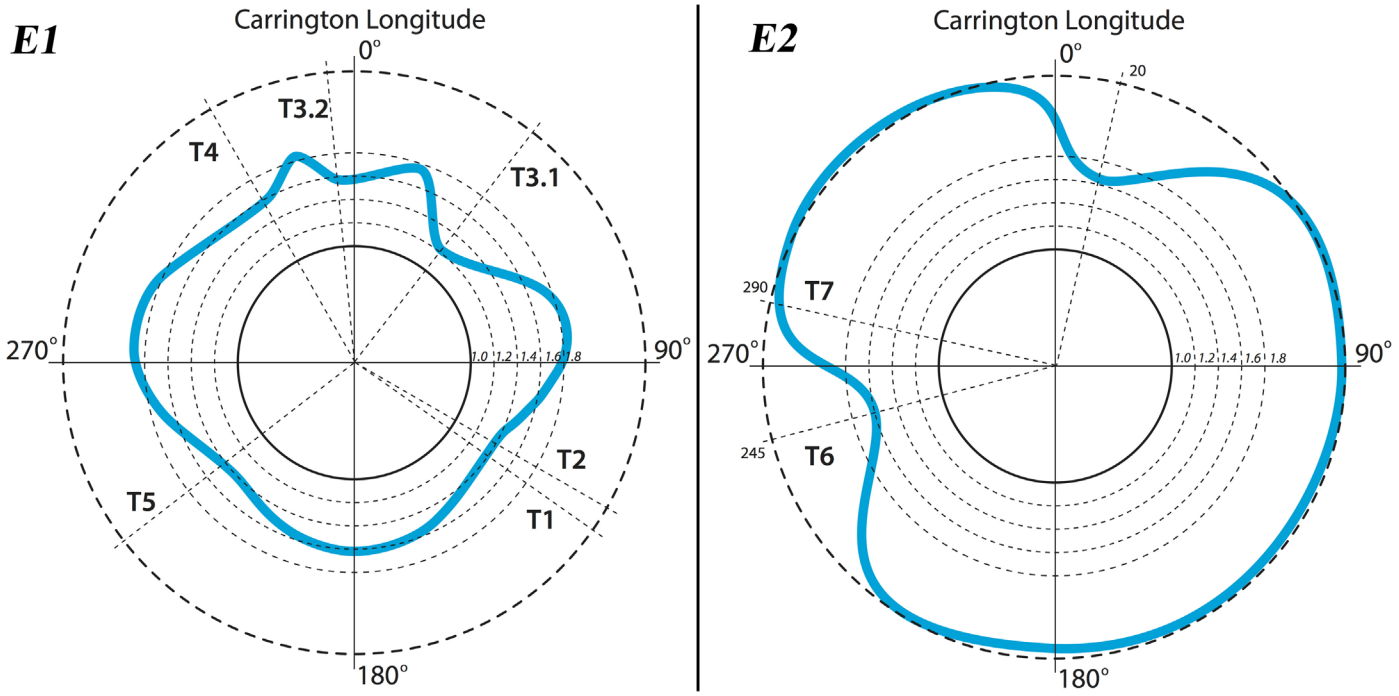

Figure 8. Longitudinal cut for the source surface height calculated from the measured photospheric magnetic field and PFSS modeling along *PSP*'s trajectory during *E1* and *E2*. The solid circle inside each panel is the Sun; the outer dashed circle has the radius of $2.5R_{\odot}$. *PSP* was moving counterclockwise from T1 to T5 during *E1*, and from T6 to T7 for *E2*.

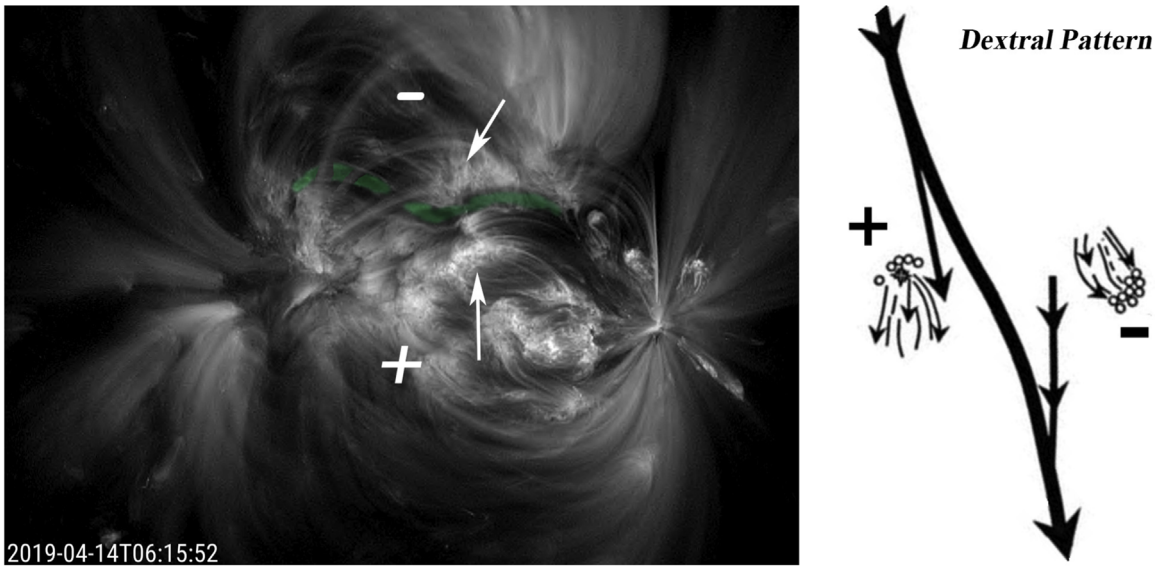

Figure 9. Active region NOAA AR 12738 with a filament (green shade) under the overlying coronal arcade with a skew corresponding to a dextral filament channel. Shown here are coronal cells on both sides of the filament (two representative cells are indicated by the white arrows): note that the cells on opposite sides of the filament channel have cusp-shaped tops that are in opposite directions. They do not cross the channel but follow the same pattern as chromospheric fibrils within a dextral filament channel as depicted in the schematic representation on the right (Panasenco et al. 2013; Sheeley et al. 2013). Coronal cells form at heights ~6–10 Mm (Sheeley & Warren 2012), much lower than average filament heights of ~50–70 Mm. The *SDO*/AIA 193 Å image is from 2019 April 14 06:15 UT.

wrinkled during *E1*, transformed into the nearly classical 2.5 $R_{\odot}$ SS during *E2*. Because these changes happened over a very short period of time between two encounters and cannot be attributed to different phases of the solar cycle, the explanation must lie in time-dependent changes in magnetic activity at the Sun in *E2*. During Encounter 2 in April 2019 the large-scale complex active region NOAA AR 12738 (with a sunspot) developed, together with a smaller but also relatively strong active region NOAA AR 12737. The active regions were separated by 120° in longitude. Such presence was sufficient to inflate the SS back to a nearly classic spherical shape with $R_{SS} = 2.5\,R_{\odot}$ except for two remaining dips. In Section 3, we use the best-fit R_{SS} height to find the solar sources of the Alfvénic slow solar wind observed at 1 au during the first *PSP* encounter and model how these regions were connected to *PSP*.

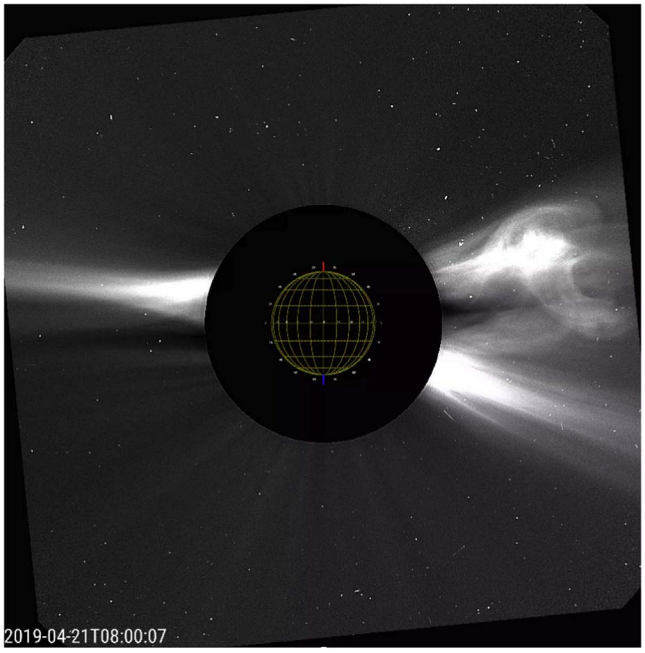

Figure 10. One of the multiple CMEs originating from NOAA AR 12738 and observed by LASCO/C2 on 2019 April 21 (a frame from the movie in the supplementary materials).

(An animation of this figure is available.)

2.1. *Influence of CMEs on* PSP *Connectivity*

During *E2*, and immediately preceding transition period T7, multiple polarity reversals were observed by *PSP* in conjunction with transient events and CMEs. Here we briefly discuss how the polarity changes associated with transient field openings from this type of event is influenced by the structure of the corresponding source filament channel on the Sun. Panasenco et al. (2013) found that the coronal cells observed and modeled by Sheeley & Warren (2012) do not cross the polarity reversal boundary within a filament channel at heights below the filament spine top. Coronal cells originate from the network field concentrations and show the same patterns as chromospheric fibrils because they follow the same filament channel magnetic topology, with a strong component of the field parallel to the photosphere. The direction of the axial field inside the filament channel and, therefore, its chirality can be deduced from the geometry of the chromospheric fibrils and coronal cells, as shown in Figure 9, illustrating active region NOAA AR 12738 and a filament channel that caused multiple CMEs. One of the CMEs is shown in Figure 10, captured by LASCO/C2. The chirality of CMEs then defines the polarity of the transient coronal hole formed on eruption and, therefore, the polarity of the field connecting to *PSP* during a CME passage. A dextral filament channel means that the direction of the axial magnetic field bears right when viewed from the positive polarity side. It means that the CME's axial magnetic field, when measured in situ by *PSP*, was directed from the positive to negative polarity parts of AR 12738. In other words, during the CME passages in 2019 April 15–22, *PSP* was momentarily connected to transient coronal holes with positive polarity. The number of positive polarity chunks in Figure 1 (bottom panel) corresponds to the number of CMEs crossing the *PSP* pass in this time period. *PSP* reaches the polarity transition period T7 only on April 22, when PFSS modeling connected *PSP* to the positive polarity of the northern corona hole extension (see Figure 7 for *E2* connectivity).

2.2. *Comparison of 3D PFSS Modeling with the LASCO/C2 Coronagraph Observations*

This section compares the PFSS extrapolations during *E1* and *E2* with LASCO C2 images to show the direct link between the neutral lines and streamers (as well as pseudostreamer stalks). The PFSS magnetogram, superposed on the (occulted) solar disk, is also shown. Figure 11 shows results for *E1*: superposition of the neighboring streamers and pseudostreamers (left panel) resulted in the merging of these two structures in coronagraph observations. However, two separate pseudostreamer stalks may be seen in the coronagraph images as thin rays. Both pseudostreamers are leaning into the equatorial streamer. Stalks are curved in both the PFSS model and white-light LASCO/C2 images, due to their weak magnetic field, lower SS heights during *E1*, and the northern coronal hole superradial expansion. Figure 12 shows the PFSS extrapolation and LASCO/C2 images for period *E2*: the open coronal field of the small coronal hole of negative polarity originating near the center of the sunspot inside active region NOAA AR 12738 coincides with the area between the streamer and pseudostreamer stalk. The active region produced multiple CMEs erupting from under the streamer, as well as multiple transients and flares with plasma propagating into the open field in the pseudostreamer environment. This might explain the apparent asymmetry in the pseudostreamer appearance at the limb, where the northern half is illuminated with more dense plasma and the southern half appears to be completely empty.

3. Analysis of the Alfvénic Slow Wind Source Regions

Throughout the first perihelion encounter, the solar wind as measured by *PSP* was dominated by large-amplitude Alfvénic fluctuations. This is well documented, e.g., in the papers by Badman et al. (2020) and Matteini et al. (2015). Quantitatively, if we define the Elsässer variables

$$z^{\pm} = \boldsymbol{v} \mp \mathrm{sign}(B_r)\boldsymbol{b}/\sqrt{(4\pi\rho)}\,,$$

where r denotes the radial component of the large-scale magnetic field B, while v and b denote velocity and magnetic field fluctuations, and ρ is the plasma density, purely outwardly propagating Alfvén waves have $z^{-} = 0$. In terms of the normalized velocity magnetic field correlation,

$$\rho_{v-b} = \frac{\boldsymbol{v}\cdot\boldsymbol{b}}{|\boldsymbol{v}\cdot\boldsymbol{b}|};$$

this means that $\rho_{v-b} = +1$ for outwardly propagating Alfvénic fluctuations along a negative polarity magnetic field line anchored at the Sun, while $\rho_{v-b} = -1$ for outwardly propagating Alfvénic fluctuations along a positive polarity magnetic field line anchored at the Sun. A state with $|z^{-}| \ll |z^{+}|$ and $|\rho_{v-b}| \geqslant 0.5$ is called Alfvénic. Additional properties of Alfvénic fluctuations are that the fluctuations of the magnetic field magnitude are much smaller than the magnetic field fluctuation amplitudes, and that relative density fluctuations are strongly suppressed with respect to the typical value in a turbulence flow, i.e., the squared turbulent Mach number.

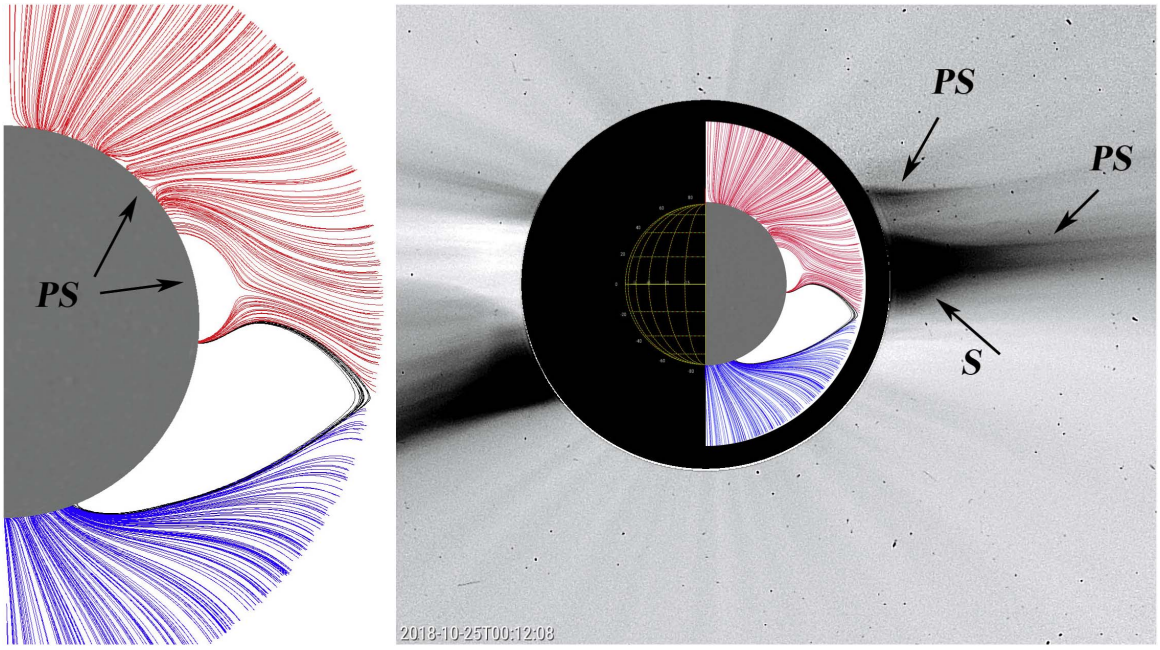

Figure 11. Left panel: solar magnetogram on disk with open magnetic field lines obtained via PFSS and $R_{SS} = 1.9\ R_{\odot}$ on 2018 October 25 00:04 UT using *SDO*/HMI data (during *E1*). The PFSS reconstructed magnetic field configuration is shown as it appears on the limb and consists of a streamer and two pseudostreamers. Right panel: a composite view of two images, one by the LASCO/C2 camera taken on 2018 October 25 00:12 UT and one of the PFSS image from the left panel. The modeled streamer and pseudostreamer positions correspond well to the ones observed by LASCO/C2.

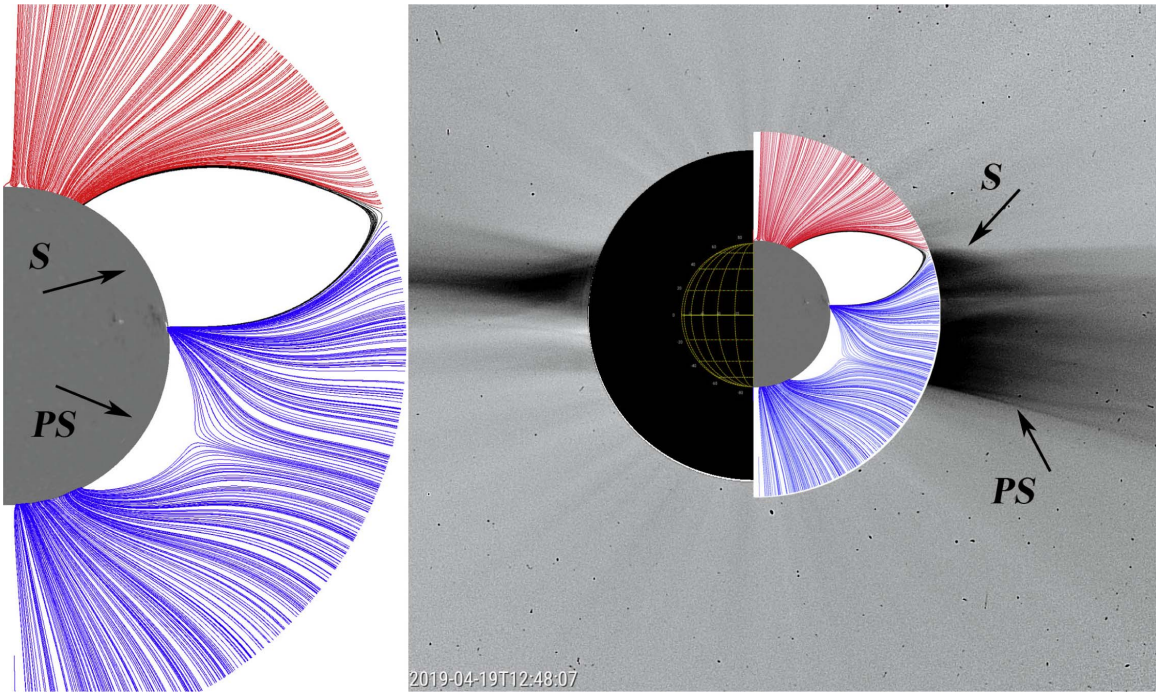

Figure 12. Left panel: solar magnetogram on disk with open magnetic field lines obtained via PFSS and $R_{SS} = 2.5\ R_{\odot}$ on 2019 April 9 12:04 UT using *SDO*/HMI data (during *E2*). The PFSS reconstructed magnetic field configuration is shown as it appears on the limb, and consists of a streamer and a pseudostreamer. Right panel: a composite view of two images, one by the the LASCO/C2 camera taken on 2019 April 19 12:48 UT and one the PFSS image from the left panel. The modeled streamer and pseudostreamer positions correspond well to the ones observed by LASCO/C2.

Figure 13 (left panel) shows solar wind measurements at 1 au over the period encompassing the first *PSP* perihelion. The left-hand side shows an interval of the slow wind detected by the Three-Dimensional Plasma and Energetic Particle Investigation (3DP; Lin et al. 1995) at ∼24 s resolution and magnetic field measurements sampled by the *WIND* Magnetic Field Investigation (MFI; Lepping et al. 1995) interpolated to the time of the plasma measurements, both on board the *WIND* spacecraft, from 2018 October 20 to 25. The upper panel displays the solar wind speed profile, V_{SW} (in km s^{-1}); in the middle panel, the *v*–*b* correlation coefficient, ρ_{v-b}, is computed at the 1 hr scale typical of Alfvénic fluctuations; the bottom panel shows the magnetic field magnitude, *B* (in nT). One sees that the velocity magnetic field correlation fluctuates strongly,

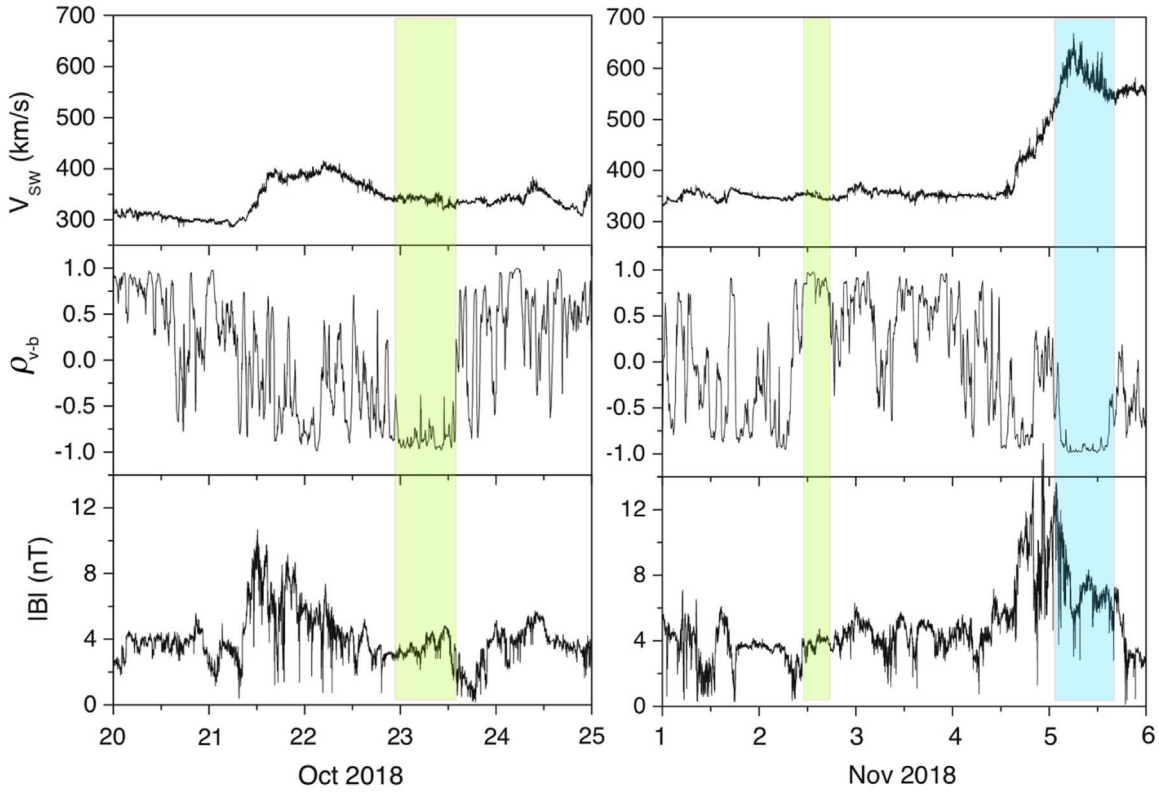

Figure 13. 1 au observations. Green shading indicates periods of Alfvénic slow solar wind in October 23 and November 2; blue area indicates Alfvénic fast wind in November 5. (Left) From top to bottom, *WIND*/3DP time series of solar wind speed, V_{SW} (in km s^{-1}); *v–b* correlation coefficient, ρ_{v-b}, computed at 1 hr scale; magnetic field magnitude, *B* (in nT) from the *WIND*/MFI instrument for the interval 2018 October 20–25. (Right) The same parameters for the interval 2018 November 1–6. The Alfvénic slow wind is highlighted in green while the fast wind is in blue.

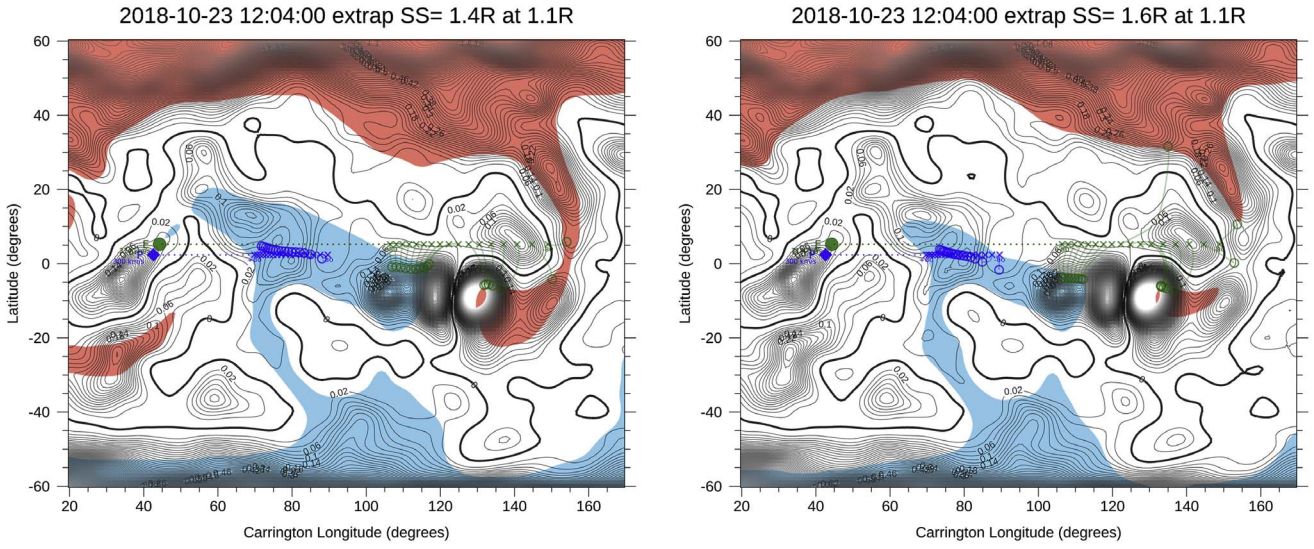

Figure 14. PFSS B^2 contour maps and solar wind footpoints for Earth's and *PSP's* trajectory for origins of the Alfvénic slow solar wind at 1 au selected in Figure 7, 2018 October 23. The projection of Earth (green circle) and *PSP* (blue diamond) on the source surface (blue crosses) and down to the solar wind source region (blue circles) calculated for the height $R = 1.1 R_{\odot}$. The maps and projections calculated for the different R_{SS}. From left to right, $R_{SS} = 1.4$ and $1.6\ R_{\odot}$ and correspond to the best-fit source surface calculated in Section 2. Open magnetic field regions shown in blue (negative) and red (positive); the neutral line is in bold.

with very few periods in which it is stably strongly either positive or negative. This interval, 2018 October 20–25, is characterized by a slow solar wind with a speed ranging between 300 and 400 km s^{-1}, and it is described by a very low *v–b* correlation coefficient overall. The most Alfvénic part is from days 23 to 23.5 with an average value of −0.87, which corresponds also to a period of almost constant magnetic field magnitude. The right-hand side of Figure 13 shows, in the same format and for the same instruments, the time series of the same parameters from 2018 November 1 to 6. In this case, the speed profile shows a transition from a slow wind characterized by a speed around 350 km s^{-1} to a stream interface followed by a

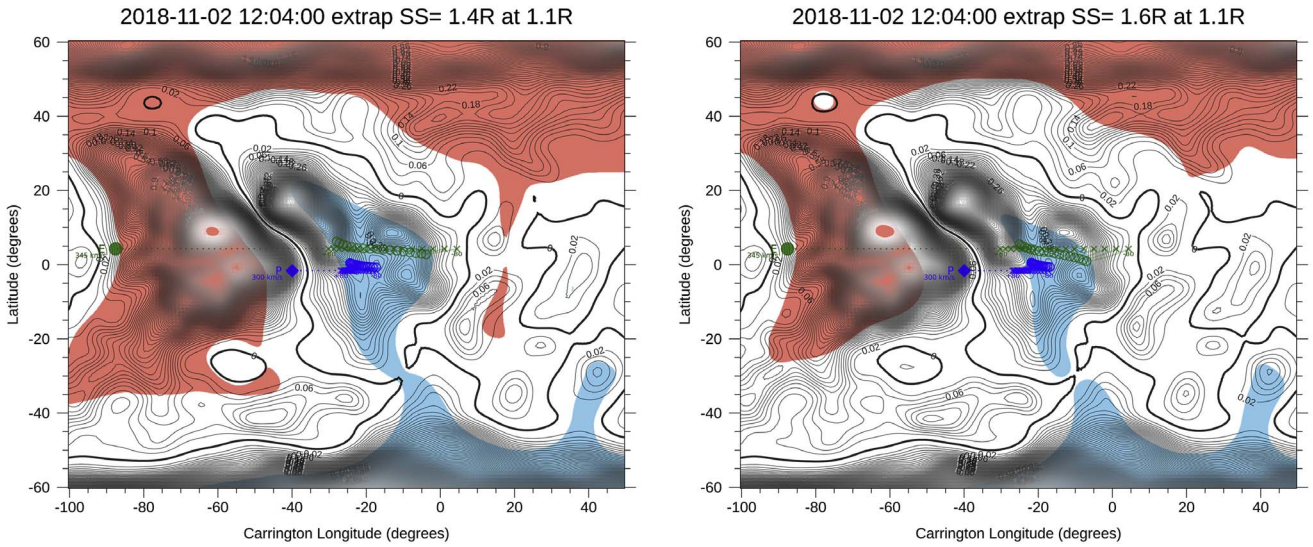

Figure 15. PFSS B^2 contour maps and solar wind footpoints for Earth's and *PSP*'s trajectory for origins of Alfvénic slow solar wind at 1 au selected in Figure 7, 2018 November 2. The projection of Earth (green circle) and *PSP* (blue diamond) on the source surface (blue crosses) and down to the solar wind source region (blue circles) calculated for the height $R = 1.1 R_{\odot}$. The maps and projections calculated for the different R_{SS}. From left to right, $R_{SS} = 1.4$ and 1.6 $R_{\odot}$ and correspond to the best-fit source surface calculated in Section 2. Open magnetic field regions shown in blue (negative) and red (positive); the neutral line is in bold.

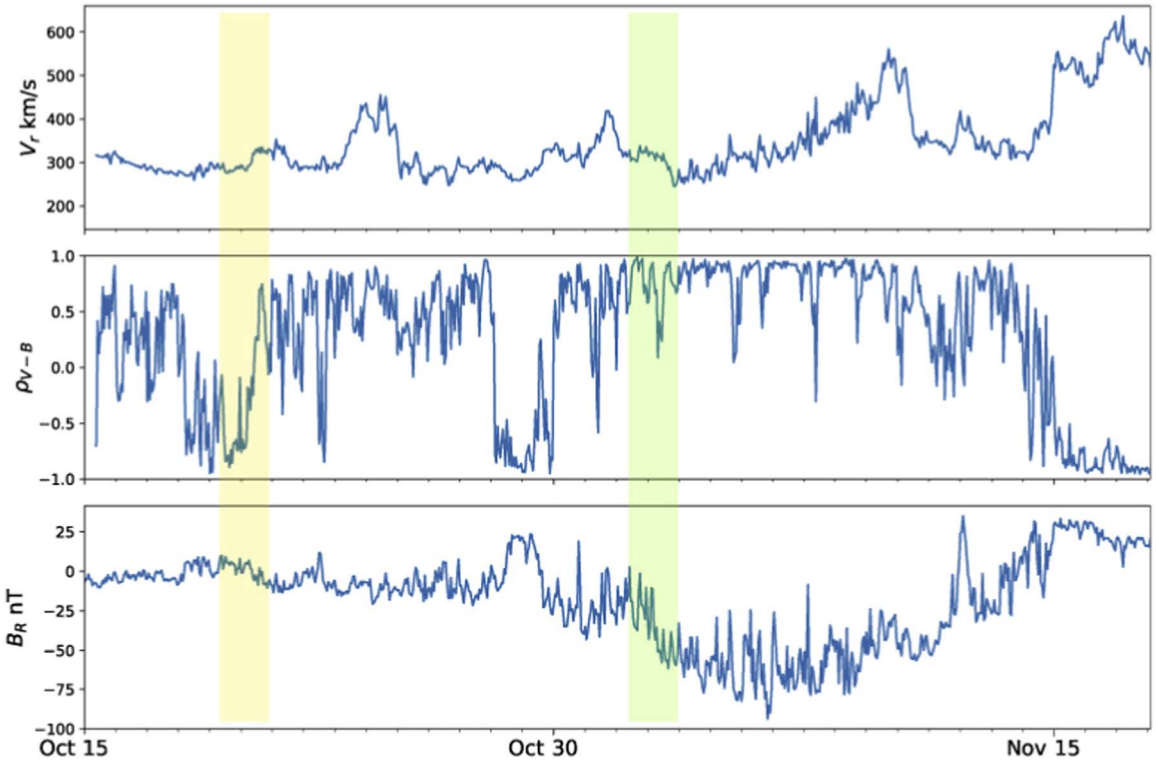

Figure 16. *PSP* observations during the interval 2018 October 15–November 18. Yellow shading indicates a period of Alfvénic slow solar wind on October 20 originating from the same region that propagated from *PSP* to 1 au to become observable at Earth (L1), where it was seen on October 23 (Figure 13, left panel and Figure 14). Green shading indicates a period of Alfvénic slow solar wind on November 2 measured at the same time at *PSP* and 1 au, when *PSP* magnetically aligned with Earth (Figure 13, right panel and Figure 15). From top to bottom, *PSP* solar wind speed, V_r (in km s^{-1}); *v*–*b* correlation coefficient, ρ_{v-b}, computed at 1 hr scale; magnetic field magnitude, B (in nT).

faster stream at the end of the interval reaching values around 600 km s^{-1}. In this case, the *v*–*b* correlation coefficient moves from values around 0 in the stream interface, where we also observe a strong compression of the magnetic field magnitude, to values around −1, in the fast wind.

To connect selected solar wind streams observed at 1 au to their sources at the Sun, we use the same method as in Section 2, when we found magnetic footpoints for the *PSP* observations of the magnetic polarity inversion periods: the spacecraft (i.e., *WIND*, or the Earth's) position to the SS is

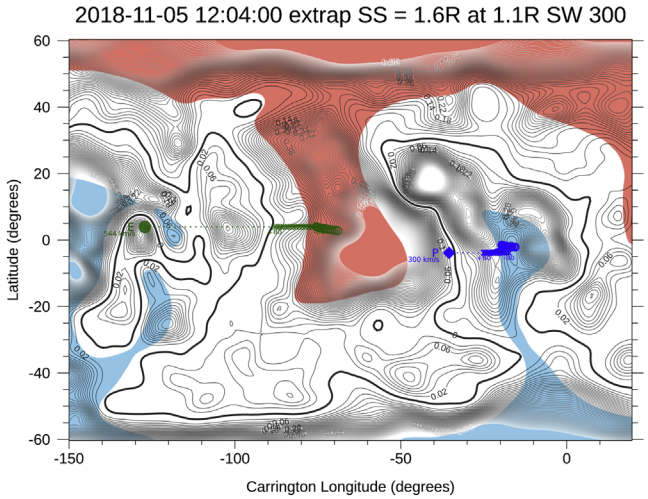

Figure 17. PFSS B^2 contour map and solar wind footpoints for Earth's and *PSP*'s trajectory for origins of Alfvénic fast solar wind stream at 1 au selected in Figure 13 (right panel; 2018 November 5). The projection of Earth (green circle) and *PSP* (blue diamond) on the source surface (blue and green crosses) and down to the solar wind source region (blue and green circles) calculated for the height $R = 1.1.R_{\odot}$. The map and projections calculated for $R_{SS} = 1.6\ R_{\odot}$ and correspond to the best-fit source surface calculated for this region in Section 2. Open magnetic field regions shown in blue (negative) and red (positive); the neutral line is in black bold.

projected via the Archimedean spiral with the given solar wind velocity, and from the SS down to the selected height above the solar surface along PFSS magnetic field lines. For each stream, the SS height determined in Section 2 for the specific region in the low solar corona is used.

Figure 14 shows the source region for the Alfvénic slow wind (measured at 1 au) plotted for two different SS radii $R_{SS} = 1.4$ and $1.6\ R_{\odot}$—the best fit and the maximum possible fit for R_{SS} as estimated from Figure 2 for this region. The projection of Earth to the SS (green crosses) and down to the height $R = 1.1.R_{\odot}$ (green circles) shows that Earth was connected over this time to positive and negative open field areas close to an activity region with a relatively strong magnetic field. As shown in Figure 13, the October 23 Alfvénic slow solar wind stream has negative ρ_{v-b}, which corresponds to a positive magnetic field. Therefore, the area from where this Alfvénic slow solar wind stream originated for this day was on the positive polarity side connecting to Earth. *PSP* observed solar wind from this area during transition period T1 in October 20 as was discussed previously in Section 2.

Figure 15 shows the same measurements but for the second Alfvénic slow wind stream observed on 2018 November 2. This Alfvénic slow solar wind stream has positive ρ_{v-b} and therefore originated from a negative magnetic polarity region on the Sun. The *PSP* magnetic footpoints were in the same area for nearly two weeks as well as on 2018 November 2, when Earth also remained connected to this area.

Figure 16 shows *PSP* measurements during the interval 2018 October 15–November 18. The three panels from top to bottom plot wind speed, the correlation ρ_{v-b}, and the radial magnetic field, respectively. Yellow shading indicates periods of Alfvénic slow solar wind on October 20th that originated from the same region on the Sun (Figures 2 and 14) and propagated from *PSP* to 1 au, arriving on October 23rd (Figure 13, left panel) when it was seen at Earth. The wind appears to undergo only a slight acceleration, from 320 to 350 km s^{-1} over the *PSP*–1 au distance. Green shading shows an Alfvénic slow wind stream at *PSP* and 1 au for 2018 November 2: this is wind from the same solar source (Figure 15), observed at the same time, and therefore different plasma parcels. A similar very slight acceleration is observed.

The Alfvénic fast solar wind stream on 2018 November 5 shown in blue in Figure 13 has a negative correlation ρ_{v-b}, and the corresponding Earth magnetic footpoints were anchored inside a positive open field area as shown in Figure 17. Earth's position extrapolates backwards into the middle of the equatorial extension of the positive northern polar corona hole. The SS where the magnetic field becomes radial was selected in accordance with the "best-fit" results described in Section 2 and was selected to be $R_{SS} = 1.6\ R_{\odot}$. Three-dimensional PFSS models in Figures 18–20 correspond to the two-dimensional magnetic pressure maps shown in Figures 14, 15, and17.

The first slow Alfvénic stream, observed on 2018 October 23 at 1 au, originated from a pseudostreamer configuration, more precisely from its southern coronal hole indicated by the black arrow in Figure 18. This is the same positive open field region shown in Figure 14 and to which Earth was magnetically connected (green circles). The very nonmonotonic expansion of the open magnetic field appears to have a funnel-like topology, similar to the geometry of the field described in Panasenco et al. (2019), which might explain its very low speed.

The second slow Alfvénic wind stream originated from an equatorial coronal hole with a relatively strong magnetic field. The very complicated topology near the base of this open field area includes multiple small-scale pseudostreamers whose branches converge and diverge in the direction perpendicular to the equator (Figure 19). On the other hand, the coronal hole from where the Alfvénic fast wind originated presented by a very smooth and monotonically expanding magnetic field (Figure 20). These results suggest that for the origin of slow Alfvénic streams, highly expanding open coronal fields are a requirement.

4. Conclusions

PSP's trajectory over its first perihelion pass brought it to traverse different regions on the Sun with different solar wind sources. A range of the solar SS heights $R_{SS} = 1.2$–$1.8\ R_{\odot}$ was required to correctly reproduce polarity transition periods during *E1*, and 1.6–2.5 for *E2*, showing that SS extrapolations generally require a nonspherical outer boundary, as illustrated in Figure 8. The SS heights above the polarity inversion regions are the local dips or minimums in the overall nonspherical SS shape during the current solar minimum.

Although the perihelion passage occurred during a time of deep solar minimum and the magnetic field on the Sun was globally very weak, different types of solar wind were observed. Around perihelion and inside corotation, *PSP* traversed a very small negative coronal hole (or coronal hole extension) prograde and retrograde, observing slow wind dominated by outwardly propagating Alfvénic turbulence throughout the encounter. It also saw faster Alfvénic wind streams before and after. The detailed properties of the waves, large-scale wave packets, including the so-called switchbacks and radial jets, are detailed elsewhere (Horbury et al. 2020; Matteini et al. 2015). Such fluctuations in the presence of extremely slow wind are not a common occurrence at greater heliocentric distances, where Alfvénic slow wind is seen more

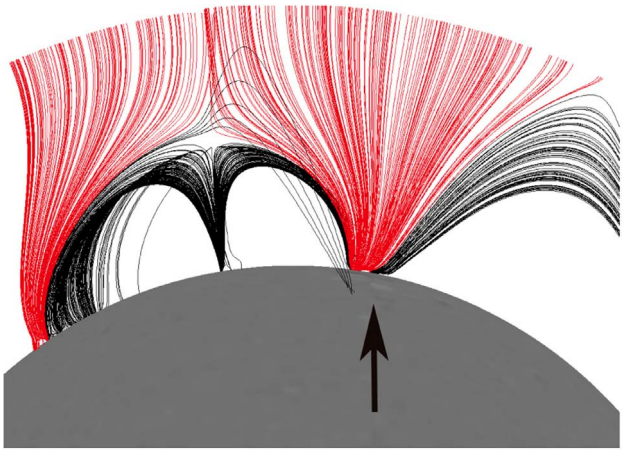

Figure 18. 3D PFSS model for the area of the origin of the Alfvénic slow solar wind observed at 1 au on 2018 October 23 (corresponds to the map in Figure 14).

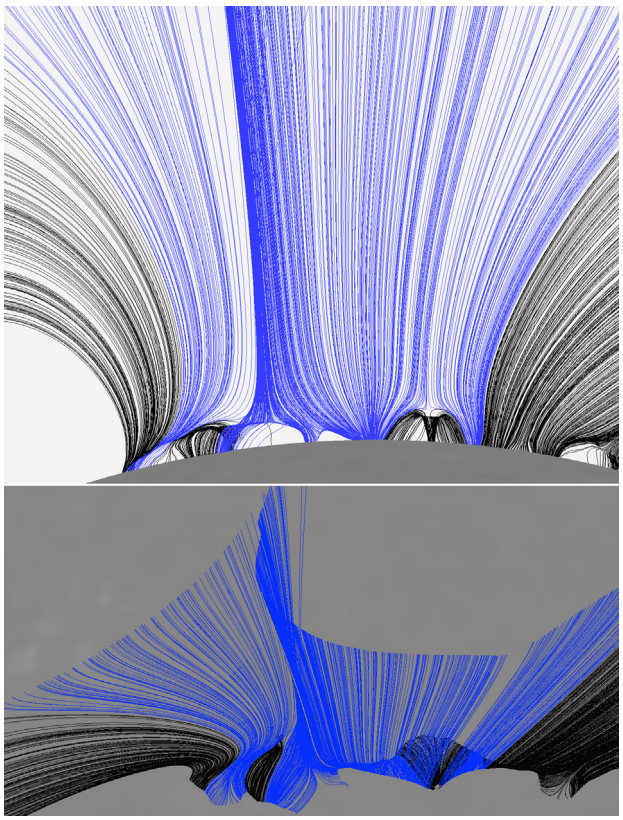

Figure 19. 3D PFSS model for the area of the origin of the Alfvénic slow solar wind observed at 1 au on 2018 November 2 (corresponds to the map in Figure 15).

commonly at solar maximum appearing to originate from so-called magnetic funnels (Panasenco et al. 2019). Here we see that the open region crossed at perihelion also has very large expansion factors, while more standard radially expanding regions remain Alfvénic with faster winds.

Using the best fit for R_{SS}, we also traced back to the Sun the short Alfvénic slow wind streams observed at 1 au, found their source regions, and created the 3D PFSS models for the coronal field in these regions. These models revealed the peculiar topology in both cases—coronal pseudostreamers at large and smaller scales. We found that only small regions of wind

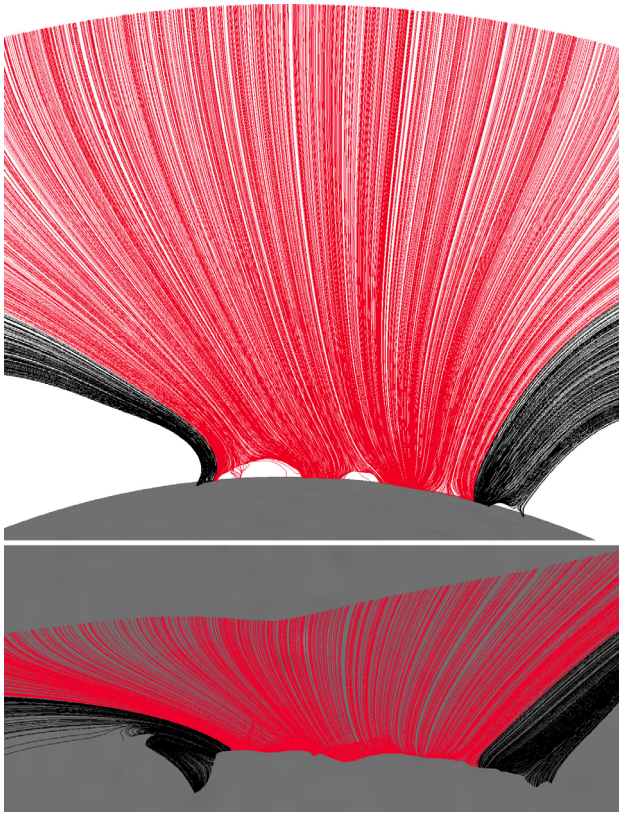

Figure 20. 3D PFSS model for the area of the origin of Alfvénic fast solar wind observed at 1 au on 2018 November 5 (corresponds to the map in Figure 17).

remained Alfvénic out to 1 au, one of which corresponded to the fast expanding open region at the *PSP* perihelion.

Our findings confirm an important property of the coronal magnetic field, namely that small regions in the corona, in the presence of complex field structures at the Sun (i.e., largely nondipolar fields) can expand superradially to occupy large regions of the heliosphere. Our findings also show that Alfvén waves may be an important part of most of the nascent solar wind, with the Alfvénicity decreasing rapidly with distance from the streams close to the equator and the heliospheric current sheet, and surviving out to greater distances only in the fast wind from dominant polar coronal holes or in the slow wind from rapidly superradially expanding small open "funnel" regions. Further research will show whether these regions, often presenting multipolar pseudostreamer configurations at their base, may be identified by other tracers, including compositional differences, in the solar wind. To this end, joint observations with the upcoming *Solar Orbiter* together with *PSP* will help to shed light on the generation and acceleration of different solar wind stream types.

O.P. was supported by the NSF EAGER grant No. 1853530. M.V. was supported by the NASA *Parker Solar Probe* Observatory Scientist grant No. NNX15AF34G. We would like to thank Marc DeRosa and Aram Panasenco for the helpful discussion on PFSS modeling. *Parker Solar Probe* was designed, built, and is now operated by the Johns Hopkins Applied Physics Laboratory as part of NASA's Living with a Star (LWS) program (contract NNN06AA01C). Support from the LWS management and technical team has played a critical role in the success of the *Parker Solar Probe* mission. Finally,

we thank the referee for their careful reading of the manuscript and timely and constructive comments.

ORCID iDs

Olga Panasenco https://orcid.org/0000-0002-4440-7166
Marco Velli https://orcid.org/0000-0002-2381-3106
Raffaella D'Amicis https://orcid.org/0000-0003-2647-117X
Chen Shi https://orcid.org/0000-0002-2582-7085
Victor Réville https://orcid.org/0000-0002-2916-3837
Stuart D. Bale https://orcid.org/0000-0002-1989-3596
Samuel T. Badman https://orcid.org/0000-0002-6145-436X
Justin Kasper https://orcid.org/0000-0002-7077-930X
Kelly Korreck https://orcid.org/0000-0001-6095-2490
J. W. Bonnell https://orcid.org/0000-0002-0675-7907
Thierry Dudok de Wit https://orcid.org/0000-0002-4401-0943
Keith Goetz https://orcid.org/0000-0003-0420-3633
Peter R. Harvey https://orcid.org/0000-0002-6938-0166
Robert J. MacDowall https://orcid.org/0000-0003-3112-4201
David M. Malaspina https://orcid.org/0000-0003-1191-1558
Marc Pulupa https://orcid.org/0000-0002-1573-7457
Anthony W. Case https://orcid.org/0000-0002-3520-4041

References

Abbo, L., Ofman, L., Antiochos, S. K., et al. 2016, SSRv, 201, 55
Antonucci, E., Abbo, L., & Dodero, M. A. 2005, A&A, 435, 699
Badman, S. T., Bale, S. D., Martinez Oliveros, J. C., et al. 2020, ApJS, doi:10.3847/1538-4365/ab4da7
Bale, S. D., Badman, S. T., Bonnell, J. W., et al. 2019, Natur, 576, 237
Bale, S. D., Goetz, K., Harvey, P. R., et al. 2016, SSRv, 204, 49
Belcher, J. W., & Davis, L. 1971, JGR, 76, 3534
Belcher, J. W., & Solodyna, C. V. 1975, JGR, 80, 181
Bruno, R., & Carbone, V. 2013, LRSP, 10, 2
D'Amicis, R., & Bruno, R. 2015, ApJ, 805, 84
D'Amicis, R., Matteini, L., & Bruno, R. 2019, MNRAS, 483, 4665
Fox, N. J., Velli, M. C., Bale, S. D., et al. 2016, SSRv, 204, 7
Geiss, J., Gloeckler, G., & von Steiger, R. 1995, SSRv, 72, 49
Horbury, T. S., Wooley, T., Laker, R., et al. 2020, ApJS, doi:10.3847/1538-4365/ab5b15
Janardhan, P., Fujiki, K., Ingale, M., et al. 2018, A&A, 618, A148
Ko, Y.-K., Roberts, D. A., & Lepri, S. T. 2018, ApJ, 864, 139
Lee, C. O., Luhmann, J. G., Hoeksema, J. T., et al. 2011, SoPh, 269, 367
Lepping, R. P., Acuña, M. H., Burlaga, L. F., et al. 1995, SSRv, 71, 207
Levine, R. H., Altschuler, M. D., Harvey, J. W., et al. 1977, ApJ, 215, 636
Levine, R. H., Schulz, M., & Frazier, E. N. 1982, SoPh, 77, 363
Lin, R. P., Anderson, K. A., Ashford, S., et al. 1995, SSRv, 71, 125
Liu, Y., Hoeksema, J. T., Scherrer, P. H., et al. 2012, SoPh, 279, 295
Marsch, E., Rosenbauer, H., Schwenn, R., et al. 1981, JGR, 86, 9199
Matteini, L., Horbury, T. S., Pantellini, F., Velli, M., & Schwarz, S. J. 2015, ApJ, 802, 11
Morgan, H. 2011, ApJ, 738, 190
Morgan, H., & Habbal, S. R. 2010, ApJ, 710, 1
Neugebauer, M., Goldstein, B. E., Smith, E. J., & Feldman, W. C. 1996, JGR, 101, 17047
Panasenco, O., Martin, S. F., Velli, M., et al. 2013, SoPh, 287, 391
Panasenco, O., & Velli, M. 2013, in AIP Conf. Proc. 1539, Solar Wind 13, ed. G. P. Zank et al. (Melville, NY: AIP), 50
Panasenco, O., Velli, M., & Panasenco, A. 2019, ApJ, 873, 25
Perrone, D., D'Amicis, R., De Marco, R., et al. 2020, A&A, submitted
Platten, S. J., Parnell, C. E., Haynes, A. L., et al. 2014, A&A, 565, A44
Scherrer, P. H., Schou, J., Bush, R. I., et al. 2012, SoPh, 275, 207
Schou, J., Scherrer, P. H., Bush, R. I., et al. 2012, SoPh, 275, 229
Schrijver, C. J., & De Rosa, M. L. 2003, SoPh, 212, 165
Schulz, M., Frazier, E. N., & Boucher, D. J. 1978, SoPh, 60, 83
Schwenn, R. 1990, in Physics of the Inner Heliosphere I—Large Scale Structure of the Interplanetary Medium, ed. R. Schwenn & E. Marsch (Berlin: Springer)
Sheeley, N. R., Martin, S. F., Panasenco, O., et al. 2013, ApJ, 772, 88
Sheeley, N. R., & Warren, H. P. 2012, ApJ, 749, 40
Stansby, D., Horbury, T. S., & Matteini, L. 2019, MNRAS, 482, 1706
Stansby, D., Matteini, L., & Horbury, T. S. 2020, MNRAS, 492, 39
Tu, C.-Y., & Marsch, E. 1995, SSRv, 73, 1
von Steiger, R. 2008, in The Heliosphere Through the Solar Activity Cycle, ed. A. Balogh, L. J. Lanzerotti, & S. T. Suess (Chichester: Springer Praxis), 41
Wang, Y.-M. 1994, ApJL, 437, L67
Wang, Y.-M., & Ko, Y.-K. 2019, ApJ, 880, 146
Wang, Y.-M., & Panasenco, O. 2019, ApJ, 872, 139
Wang, Y.-M., & Sheeley, N. R. 1990, ApJ, 365, 372
Wang, Y.-M., Sheeley, N. R., Jr., & Rich, N. B. 2007, ApJ, 658, 1340
Zhao, L., Zurbuchen, T. H., & Fisk, L. A. 2009, GeoRL, 36, L14104